

# Detecting the Wind-Driven Shapes of Extrasolar Giant Planets from Transit Photometry

Jason W. Barnes

*Department of Physics  
University of Idaho  
Moscow, ID 83844-0903  
jwbarnes@uidaho.edu*

Curtis S. Cooper<sup>1</sup>, Adam P. Showman, William B. Hubbard

*Department of Planetary Sciences  
University of Arizona  
Tucson, AZ 85721*

## ABSTRACT

Several processes can cause the shape of an extrasolar giant planet's shadow, as viewed in transit, to depart from circular. In addition to rotational effects, cloud formation, non-homogenous haze production and movement, and dynamical effects (winds) could also be important. When such a planet transits its host star as seen from Earth, the asphericity will introduce a deviation in the transit lightcurve relative to the transit of a perfectly spherical (or perfectly oblate) planet. We develop a theoretical framework to interpret planet shapes. We then generate predictions for transiting planet shapes based on a published theoretical dynamical model of HD189733b. Using these shape models we show that planet shapes are unlikely to introduce detectable lightcurve deviations (those  $> 1 \times 10^{-5}$  of the host star), but that the shapes may lead to astrophysical sources of systematic error when measuring planetary oblateness, transit time, and impact parameter.

*Subject headings:* techniques:photometric — eclipses — planets and satellites: individual: HD189733b — planets and satellites: individual: HD209458b

## 1. INTRODUCTION

Transits are proving to be the key to characterizing extrasolar giant planets. Transit lightcurve photometry has allowed measurements of planets' orbital inclination and radius, which when combined with radial velocity observations allows an unambiguous determination of a planet's mass and density. To date such measurements have been made for 55 transiting planets (for an up-to-date list of known transiting planets see the Extrasolar Planets Encyclopedia at <http://exoplanet.eu/catalog-transit.php/>).

Previous groups have suggested that visible-light transit photometry could determine a planet's oblateness (Seager & Hui 2002; Barnes & Fortney 2003), the existence of ring systems (Barnes & Fortney 2004), and/or the potentially artificial nature of the transiting object (Arnold 2005). However, the published lightcurves of each of the transiting planets discovered thus far indicate no deviations from sphericity within errors. Infrared observations of transiting planets' secondary eclipse has revealed the dayside brightness temperature of TRES-1 (Charbonneau et al. 2005), HD209458b (Deming et al. 2005; Knutson et al. 2008) and HD189733b (Deming et al. 2006; Charbonneau et al. 2008; Grillmair et al. 2008) and

the spectrum of HD209458b (Richardson et al. 2007; Swain et al. 2008) and HD189733b (Grillmair et al. 2007).

Numerical simulations of atmospheric dynamics predict that the photospheres of hot Jupiters are non-homogenous (Cho et al. 2003; Cooper & Showman 2005; Langton & Laughlin 2007; Dobbs-Dixon & Lin 2008; Showman et al. 2009b). The longitudinal structure of these thermal variations was predicted to be detectable using infrared photometry over the course of a full orbit (Fortney et al. 2006) and may also be detectable during the planet's ingress and egress from secondary eclipse (Williams et al. 2006; Rauscher et al. 2007). Recent *Spitzer* Space Telescope measurements have shown phase-dependent infrared flux variability for  $\nu$  Andromedae (Harrington et al. 2006) and HD189733 (Knutson et al. 2007, 2009). These measurements provide the first constraints for dynamical models; however, the measured phase function does not match that predicted theoretically.

In this paper, we show that atmospheric dynamics also introduces asphericity to a transiting planet's observed shape, but that the lightcurve deviations thus produced are likely too small to be detected. First we investigate the processes that might affect a planet's shape (Section 2). Next we derive an analytical expression for a planet's shape in the simplified case of modification by a param-

eterized eastward equatorial jet (Section 3). We then develop a theoretical framework for the effects of planet shape on transit lightcurves numerically using hypothetical regularly-shaped planets as a guide (Section 4). Finally we calculate the predicted shape of HD189733b based on the new dynamical models of Showman et al. (2009b) (Section 5), and calculate the transit lightcurves for the predicted planet shape models, discussing shape detectability from ground- and space-based photometry.

## 2. PLANET SHAPE THEORY

The radius of a planet viewed in transit corresponds to the radius at which the slant optical depth of the planet's atmosphere is sufficient to block all potentially transmitted light, which varies with the wavelength of observation (Seager & Sasselov 2000). In general, this measured transit radius can differ substantially from the nominal 1-bar-pressure radius used in planetary evolution calculations due to molecular absorptions, clouds, Rayleigh scattering, or refraction (Hubbard et al. 2001; Burrows et al. 2003; Hui & Seager 2002a). The long slant optical path through a transiting planet's outer atmosphere leads to total optical depths between 35 and 90 times greater than the normal optical depth. Hence seemingly unimportant condensates or hazes can drive the transit radius to pressures as low as 1 millibar (Fortney 2005). With an atmospheric pressure scale height near 500 km for HD209458b (Hubbard et al. 2001), this effect would lead to a difference of  $\sim 5000$  km, or  $\sim 5\%$  between the measured transit radius and the planet's 1-bar-pressure radius.

Most previous studies have treated transiting planets as either perfectly spherical (*e.g.* Hubbard et al. 2001) or perfectly oblate (Hui & Seager 2002b; Seager & Hui 2002; Barnes & Fortney 2003). However, inhomogeneities in either the lateral or elevational distribution of molecular absorbers or condensates (clouds and hazes) can lead to the departure of a planet's shape from that of a sphere as measured in transit. Iro et al. (2005) calculated that the day-night temperature contrast on HD209458b could lead to an asymmetry in the abundance of sodium between the morning and evening limbs of the planet as viewed in transit, though Cooper & Showman (2006) showed that carbon monoxide should be distributed uniformly due to chemical disequilibrium effects.

Three-dimensional dynamical simulations predict areas of upwelling, downwelling, and horizontal jets on close-in extrasolar giant planets (Showman & Guillot 2002; Cooper & Showman 2005). Vigorous dynamics of the type predicted are consistent with the formation of clouds if condensates are available and if the atmospheric pressure-temperature profile is appropriate (Sudarsky et al. 2000; Cooper et al. 2003; Fortney et al. 2005). However, to date no predictions of cloud cover patterns have been made for extrasolar planets.

In addition to the possible creation of cloud bands, atmospheric dynamics can directly affect a planet's transit shape by changing the constant-density surfaces. At a

given gravitational equipotential surface, thermodynamic variations driven by insolation, radiation, and air movement result in variations in air density. High-speed jets are particularly effective.

Assuming that the atmospheric opacity is proportional to density, as would be the case if the opacity resulted from refraction, Rayleigh scattering, molecular absorption, and possibly condensate particulates, the  $\tau = 1$  height as a function of azimuthal location on the planet's disk would follow the constant-density surfaces. If the constant-density surfaces deviate from an equipotential surface, the deviant shape would alter the planet's transit lightcurve.

## 3. ANALYTICAL WIND-DRIVEN SHAPES

We quantify the dynamical shape deviations analytically to estimate the intensity of the effects of a steady-state, idealized zonally symmetric jet. We assume that the vertical and north-south wind speeds are zero. While realistic atmospheres will be decidedly more complex, these assumptions allow us to derive an analytic toy model that will aid in understanding the more realistic cases that we analyze in Section 5.

We start with the north-south component of the horizontal momentum equation from atmospheric dynamics (*e.g.*, Holton 2004):

$$\frac{dv}{dt} = -fu - \frac{\partial \Phi(P, \phi)}{\partial y} - \frac{u^2 \tan \phi}{a} \quad (1)$$

where  $u$  is the eastward zonal wind speed,  $v$  is the northward meridional wind speed,  $\phi$  represents the latitude,  $a$  is the planet's radius,  $y$  is the northward distance on the sphere centered on the planet with radius  $a$ ,  $f$  is the coriolis parameter defined to be  $f \equiv 2\Omega \sin \phi$ ,  $\Phi$  is the gravitational potential relative to that of an oblate spheroid (*i.e.*, not including the centrifugal term) and  $\Omega$  is the planet's rotation rate in radians per second. Assuming a jet in gradient-wind balance (*i.e.* a 3-way balance between Coriolis, centrifugal, and pressure-gradient forces) with an assumption of zero meridional wind (a good approximation even for solar system planets), then  $\frac{dv}{dt}$  is zero, leaving us with

$$\frac{\partial \Phi}{\partial y} = -fu - \frac{u^2 \tan \phi}{a}. \quad (2)$$

We then integrate to determine  $\Phi(\phi, P)$ , where  $P$  refers to the atmospheric pressure,

$$\Phi = \int \frac{\partial \Phi}{\partial y} dy \quad (3)$$

where  $y = a\phi$ . We assume a simple wind field  $u(\phi)$  as a function of latitude ( $\phi$ ) with the winds zero at the poles,  $u_0$  at the equator, and varying sinusoidally in the mid-latitudes:

$$u = u_0 \cos(\phi). \quad (4)$$

While not rigorously realistic, this north-south wind profile allows us to derive an analytic solution while bearing at least superficial resemblance to the superrotating

equatorial jets predicted for hot Jupiters using 3D models (Showman & Guillot 2002; Cooper & Showman 2005; Showman et al. 2009a; Dobbs-Dixon & Lin 2008). While solar system planets have more complex zonal wind structures, hot Jupiters are predicted to have a single broad jet similar to the one modeled. Use of double-angle formulae, integration, and simplification results in:

$$\Phi(\phi) - \Phi_0 = \frac{u_0}{2} \left( \frac{u_0}{2} + \Omega a \right) \cos(2\phi') \Big|_{\phi'=\phi}. \quad (5)$$

We assume that the jet is hydrostatically balanced and that the vertical temperature profile is isothermal along the reference trajectory. The isothermal assumption allows us to arrive at an analytical solution, but we do not expect the shape of a non-isothermal planet to differ significantly from the analytical solution thus derived. We further assume that the gas behaves ideally, *i.e.* that  $\rho = \frac{P}{RT_0}$ . The constant  $\Phi_0$  represents the reference potential at latitude  $\phi_0$ ,

$$\Phi_0 = \Phi_{\text{ref}} - RT_0 \ln\left(\frac{P}{P_{\text{ref}}}\right). \quad (6)$$

We take  $\Phi_0$  to be equal to the true gravitational potential  $\Phi_{\text{ref}}$  when  $\phi_0 = 0$  (*i.e.*, the equator). Evaluating Equation 5 then results in:

$$\Phi(\phi) = \frac{u_0}{2} \left( \frac{u_0}{2} + \Omega a \right) (\cos(2\phi) - 1) + \Phi_0. \quad (7)$$

The effective gravitational potential as a function of pressure ( $P$ ) is then:

$$\Phi(\phi, P) = \frac{u_0}{2} \left( \frac{u_0}{2} + \Omega a \right) (\cos(2\phi) - 1) + RT_0 \ln\left(\frac{P}{P_{\text{ref}}}\right) - \Phi_{\text{ref}}. \quad (8)$$

Using the ideal gas law this becomes

$$\Phi(\phi, \rho) = \frac{u_0}{2} \left( \frac{u_0}{2} + \Omega a \right) (\cos(2\phi) - 1) - RT_0 \ln\left(\frac{\rho RT_0}{P_{\text{ref}}}\right) - \Phi_{\text{ref}}. \quad (9)$$

To solve for the magnitude of the resulting atmospheric-dynamics-induced shape change for the planet, we look at the difference in magnitude of the polar and equatorial potentials,

$$\Delta\Phi \equiv \Phi(\phi = 0) - \Phi(\phi = \frac{\pi}{2}). \quad (10)$$

Substituting in for the latitude values and assuming a constant-density surface we arrive at

$$\Delta\Phi = u_0 \left( \frac{u_0}{2} + \Omega a \right), \quad (11)$$

which leads to an equator-to-pole radius difference of

$$r_{\text{eq}} - r_{\text{p}} = \frac{u_0}{g} \left( \frac{u_0}{2} + \Omega a \right) \quad (12)$$

when we divide by the local acceleration due to gravity,  $g$ .

For a jet on HD209458b of 1 km/sec, similar to the rotational speed at the planet's equator, Equation 12 predicts a modest wind-induced equator-to-pole radius difference of 82 km. A wind-induced shape change of this magnitude

would be comparable to that induced by the planet's rotation (Barnes & Fortney 2003), and thus difficult to discern for this (probably) tidally-locked planet.

From numerical atmospheric circulation models, Cooper & Showman (2005) simulate a robust eastward jet for HD209458b with velocity of 2.8 km/s at the 20-bar pressure level, and 4 km/s at 220 millibars' pressure, similar to the results of other models (Showman et al. 2008). Substituting in these values for  $u_0$  in Equation 12 yields wind-induced equator-to-pole radius differences of 480 km and 960 km respectively. These numerically-derived wind speeds would imply a planet shape difference comparable to HD209458b's atmospheric scale height of 440 km (*e.g.*, Fortney 2005), and might therefore be detectable. If the planet's slant optical depth (Fortney 2005) is such that the pressure-level probed in transit is very high in the atmosphere, the shape could be even more exaggerated.

Showman et al. (2009b) have more sophisticated coupled radiative-dynamical simulations for extrasolar planet HD189733b. These simulations show a qualitative similarity to those of Cooper & Showman (2005) in that they predict a strong west-to-east equatorial jet. The Showman et al. (2009b) model shows a maximum wind speed of  $\sim 3.5$  km/s at 10 millibars' pressure. From this wind speed, equation 12 predicts a wind-induced equator-to-pole shape difference of 715 km for HD189733b at 10 millibars.

#### 4. PLANET SHAPE MEASUREMENT

The newly-launched *Kepler* mission can measure lightcurves to strikingly high precision (Borucki et al. 2009). The measurement precision for the parent star of planet HAT-P-7b ( $V=10.5$ ) is  $6 \times 10^{-5}$  per half-hour data point. But the real power for detecting small lightcurve deviations from *Kepler* will come from the coaddition of a whole sequence of transits. In the HAT-P-7b case, for instance, there will be a total of 580 transits during the *Kepler* prime mission because of the planet's 2.2-day orbital period. By coadding those into a single lightcurve, the effective precision can be reduced by a factor of 24 to just  $2.5 \times 10^{-6}$  per half-hour measurement, or alternatively about  $1.4 \times 10^{-5}$  for each 1-minute measurement (assuming that this star is put onto the short-cadence list). Hence lightcurve deviations at the 10 parts-per-million level may eventually be detected by *Kepler* by its end of mission.

In order to determine whether or not wind-induced departures from sphericity should be detectable, we now numerically approach the problem of the effects of shape on transit lightcurves.

The lightcurves of all of the transiting planets known to date are well-modeled by fitting just four values (assuming a value for the stellar mass): the stellar radius ( $R_*$ ), the planetary radius ( $R_p$ ), the transit impact parameter ( $b$ , the distance between the projected centers of the planet and star at mid-transit, in units of  $R_p$ ), and one or more parameters describing stellar limb darkening (*e.g.*,

$c_1$ , (Barnes & Fortney 2003)). If a planet is not a perfect sphere, and if the deviation is large enough, then its transit lightcurve would not be adequately modeled with this type of 4-parameter fit. Hence the residual from the 4-parameter spherical planet fit provides a measure of the photometric detectability of deviations from a spherical planet (Barnes & Fortney 2003).

Deviations from either planetary sphericity (Seager & Hui 2002; Barnes & Fortney 2003, 2004; Arnold 2005) or uniform orbital motion (Barnes 2007) lead to lightcurve residuals that are largest during planets' transit ingress and egress. Dynamically-driven deviations ought to be most detectable near ingress and egress as well.

To establish a systematic framework within which realistic deviations can be understood, we first investigate the detectability of hypothetical planets with regularly-varied shapes. Specifically we look at planets whose azimuthal profiles as seen in transit vary as

$$r(\theta) = R_p + A \sin(n\Theta + \Psi) \quad (13)$$

where  $r$  is the projected planetary radius as a function of the azimuthal angle  $\Theta$  and  $A$  is a constant with dimensions of length that corresponds to the amplitude of the deviation (Figure 1). The parameter  $\Psi$  represents a phase factor and affects the orientation of the resulting figure. The positive-integer-valued  $n$  allows for the generation of planets with varying numbers of crenulations.

The set of all shapes  $r_n(\theta)$  with  $\Psi = 0, \pi/2$  provides an orthonormal basis that spans the space of possible planet shapes. Since any arbitrary planet shape can be represented as a sum of shapes of the form  $r_n(\theta)$ , understanding the lightcurves of these basic shapes will elucidate the nature of the lightcurves of more complex objects.

We calculate transit lightcurves using the method of (Barnes & Fortney 2004): an explicit numerical integration of the light blocked by the planet relative to the total stellar flux. This calculation is makes no approximations regarding stellar limb darkening. Only computational time and double-floating-point precision limit its accuracy. We fit these artificial lightcurves with a spherical planet

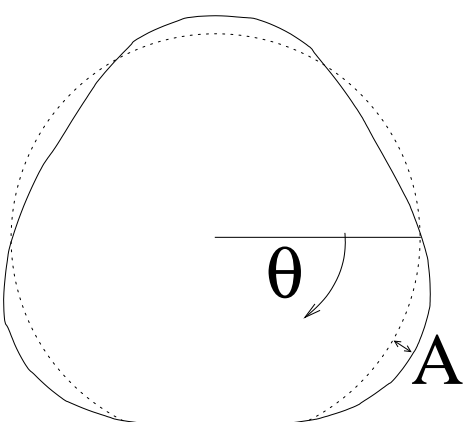


Fig. 1.— Geometry of shape parameterization.

model using a Levenberg-Marquardt algorithm to arrive at a least-squares-minimizing fit. As in Barnes & Fortney (2004), we fit for the parameters  $R_*$ ,  $R_p$ ,  $b$ , and the limb darkening parameter  $c_1$  as defined in (Brown et al. 2001).

The lightcurve residuals, after having been fit with the spherical-planet model, for hypothetical transiting planets with  $n = 2, 3, 4, 5, 6$  are shown in Figures 2 and 3. Figure 2 shows the residuals for planets that are symmetric around a vector corresponding to their orbit normal; Figure 2 shows planets that are asymmetric with respect to their orbit normal. Symmetric planets that transit generate lightcurves that are symmetric with respect to the mid-transit time. The asymmetric planets generate antisymmetric lightcurves due to the nature of their asymmetry.

The  $n = 1$  case (not shown) corresponds to planets whose center-of-mass is offset from their projected center-of-figure. The best-fit spherical planet model parameter for this case have small systematic errors resulting from the offset, but their lightcurve residuals are negligible.

The two-lobed case ( $n = 2$ ) forms an opaque ellipse in projection. This kind of shape might resemble that formed by a giant planet with a single strong prograde equatorial jet. In its transit lightcurve, such a planet behaves like an oblate planet. Barnes & Fortney (2003) showed that these planets show a distinct transit residual with one positive and one negative peak during ingress and egress. Oblate planets show a reduced signature for symmetric transits (Figure 2) relative to oblate planets with antisymmetric transits due to variations in the spherical model fit parameters that act to mimic the oblate transit signature.

Residuals for shapes with  $n > 2$  become progressively more complex. These higher-order shapes show a number of positive and negative deviations during ingress and egress. Empirically, as can be seen in Figures 2 and 3, the number of peaks in the residual during planet ingress and egress is equal to  $n$ . As the length of ingress and egress is not a function of  $n$ , the duration of each deviation becomes progressively shorter as  $n$  increments. Hence complex, higher-order shapes would require a faster cadence for photometric observations in order to be detected.

In the antisymmetric case (Figure 3), the amplitude of the peaks in the lightcurve residual decreases with increasing  $n$ . Hence detecting higher-order shapes requires better photometric precision than lower-order ones. The symmetric case is similar, with the exception of  $n = 2$  which has relatively low detectability due to the spherical planet fit, as described above.

## 5. APPLICATION TO HD189733b

Non-spherical planet shapes could be detectable with transit photometry, then, given a large enough amplitude for the deviations from sphericity. To test whether the effect should be seen for known extrasolar planets, we estimate the shape of transiting planets HD189733b using the Showman et al. (2009b) SPARC/MITgcm atmo-

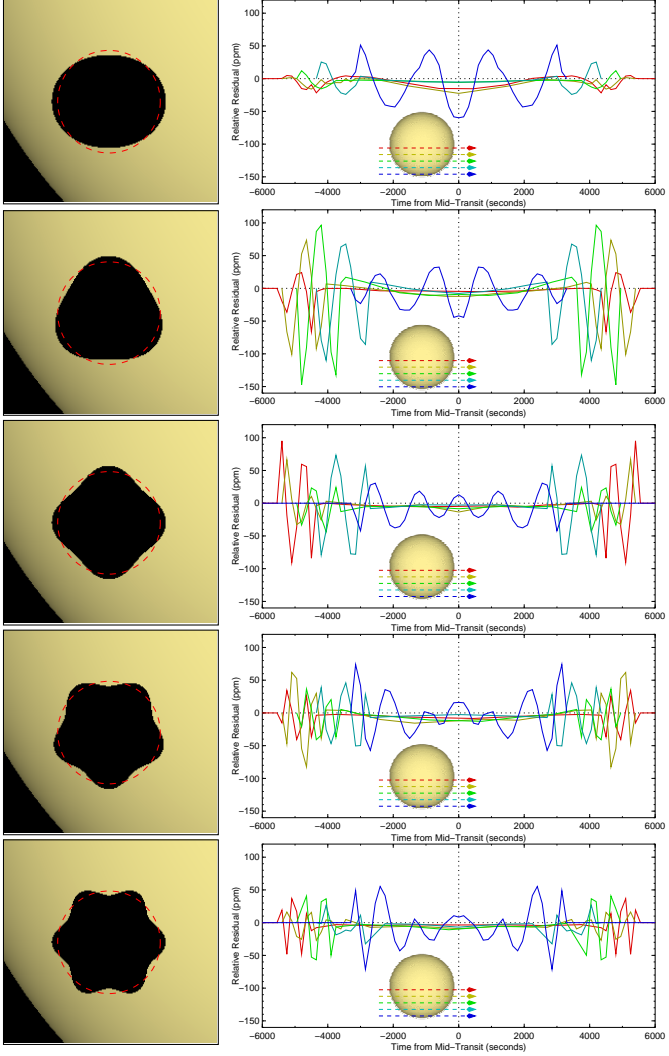


Fig. 2.— Lightcurve fit residuals for regularly-shaped planets that are symmetric with respect to their orbit normal. From top to bottom they have (see Equation 13):  $n = 2$ ,  $\Psi = \pi/2$ ;  $n = 3$ ,  $\Psi = 0$ ;  $n = 4$ ,  $\Psi = \pi/2$ ;  $n = 5$ ,  $\Psi = 0$ ; and  $n = 6$ ,  $\Psi = \pi/2$ . The color for each lightcurve residual is colored such that red corresponds to impact parameter  $b = 0.1$ , yellow to  $b = 0.3$ , green to  $b = 0.5$ , cyan to  $b = 0.7$ , and blue to  $b = 0.9$ . The flux show is plotted relative to the total stellar flux. This hypothetical planet has a radius equal to that of Jupiter and orbits a  $1 M_\odot$  star with the same limb darkening as HD209458b with a semimajor axis of 1 AU. To convert to other semimajor axes, multiply the x-axis by  $\text{sqrt}a_p$  where  $a_p$  is the planet's semimajor axis in astronomical units. The value of  $A$  used here is  $0.1 R_{\text{Jup}}$ . The amplitude of the transit residual is proportional to  $A$  for  $A \ll R_p$ .

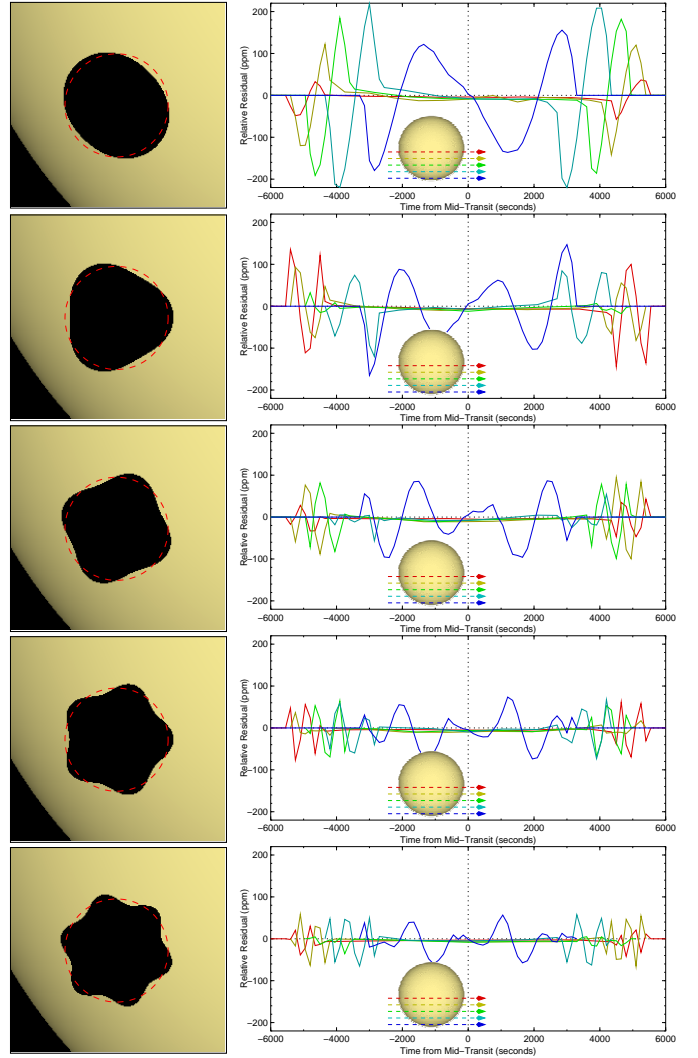


Fig. 3.— Lightcurve fit residuals for regularly-shaped planets that are asymmetric with respect to their orbit normal. From top to bottom they have (see Equation 13):  $n = 2$ ,  $\Psi = 0$ ;  $n = 3$ ,  $\Psi = \pi/2$ ;  $n = 4$ ,  $\Psi = 0$ ;  $n = 5$ ,  $\Psi = \pi/2$ ; and  $n = 6$ ,  $\Psi = 0$ . The color for each lightcurve residual is colored such that red corresponds to impact parameter  $b = 0.1$ , yellow to  $b = 0.3$ , green to  $b = 0.5$ , cyan to  $b = 0.7$ , and blue to  $b = 0.9$ . To convert to other semimajor axes, multiply the x-axis by  $\text{sqrt}a_p$  where  $a_p$  is the planet's semimajor axis in astronomical units. The value of  $A$  used here is  $0.1 R_{\text{Jup}}$ . The amplitude of the transit residual is proportional to  $A$  for  $A \ll R_p$ .

spheric model. To arrive at a planet shape, we assume that the slant optical depth of the planet's atmosphere is unity where the density is  $2.2 \times 10^5 \text{ kg m}^{-3}$ . The resulting shape is shown in Figure 4.

The SPARC model predicts a total variation in shape of  $\sim 700 \text{ km}$ . This value agrees very well with the theoretical value derived in Section 3 (715 km).

In order to predict the lightcurve effects of this model-predicted shape, we create a simulated transit lightcurve that we then fit with a spherical-planet model, as we did for hypothetical regularly-shaped planets in Section 4. The lightcurve residuals that result are decidedly too small to be measured – less than 1 part in  $10^5$  of the stellar flux.

To understand why the wind-driven shape is so hard to detect, we compare the model HD189733b shape with the numerical results from Section 4. Since for small deviations from a sphere the detectabilities of various planet shapes are linear with respect to the shapes themselves, the detectability for the model HD189733b should be the same as a linear combination of the regular planet shapes from Section 4. We determine the relative contributions of each regular shape by taking the Fourier transform of the predicted model shape shown in Figure 4. The results are in Table 1.

While the dynamical model predicts the total equator-to-pole radius difference to be of order 700 km (which would correspond to an amplitude of 350 km from Table 1 if it were all in one component), the Fourier components in Table 1 show that the majority of the amplitude is in the  $\Psi = \pi/2$  symmetric components.

The  $n = 1$  component corresponds to an offset between the planet's center of mass and its center of figure. This component is inherently undetectable using transit photometry alone, as it is sensitive only to the figure and not to the planet's mass. The  $n = 2$  symmetric component corresponds to the planet's oblateness. As shown in Figure 2 (and in Barnes & Fortney (2003)), this component has a relatively low detectability owing to the ability of a spherical planet model to partially emulate the oblate

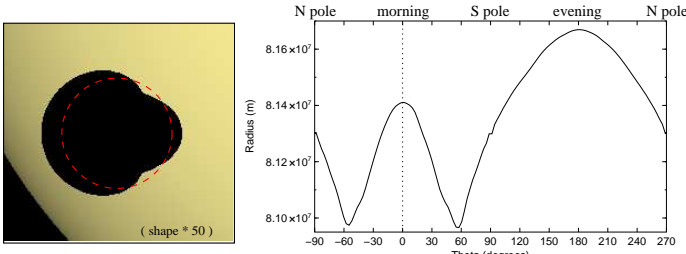


Fig. 4.— Predicted wind-driven shape of HD189733b presented as an image (left; exaggerated 50 times) and as a graph (right). The average radius has been forced to the measured value,  $1.138 R_{\text{Jup}}$ . The dashed red line at left corresponds to the location and size of a spherical  $1.00 R_{\text{Jup}}$  planet with the same center of mass as HD189733b for purposes of comparison.

planet's transit lightcurve. The higher-order components,  $n = 3, 4, 5, 6$ , have progressively lower inherent detectabilities and lower Fourier amplitudes in the dynamical model prediction as well, leading to their having very small effects on the planet's transit lightcurve.

Though the raw wind speeds predicted for hot Jupiters would appear to lead to detectable shape amplitudes, the nature of the shapes that result are such that the detectability is low. Hence wind-driven shapes of extrasolar planets are unlikely to be detectable in transit photometry barring unusual high-velocity zonal wind structures. It remains possible that clouds or spatial variations in the intensity of haze or molecular absorption could create unusual shapes with amplitudes large enough to be detected in some cases.

If a transiting planet had a nonzero obliquity, then even a symmetrically uniform wind jet would introduce a much more detectable antisymmetric lightcurve. However, in order for a planet not to have its obliquity reduced to near zero by tides, that planet would necessarily need to be far from its parent star. At those large distances, the stellar insolation available to drive winds is lower, and hence we might expect a smaller amplitude for the wind-driven shape (though nobody has modeled such a situation yet). The net detectability may be higher, though, due to the presence of antisymmetric Fourier components.

## 6. CONCLUSION

Planetary winds affect the three-dimensional shape of a planet's constant-density contours, leading to departures from sphericity. A planet's silhouette as viewed in transit should depend on the projected shape of these constant-density surfaces, assuming that absorption depends only on atmospheric density. The resulting silhouette should affect the planet's transit lightcurve.

We calculate an analytical estimate for the amplitude of the shape variation, using simplifying assumptions regarding a planet's zonal wind structure. Using the maximum equatorial winds found in dynamical models of HD209458b (Cooper & Showman 2005) predicts an atmospheric-dynamics-driven global equator-to-pole radius difference of between 480 km and 960 km. Using results from the more sophisticated Showman et al. (2009b) model of HD189733b, the analytic expression predicts a 715 km atmospheric-dynamics-driven global equator-to-pole radius difference.

For a more robust estimate of a planet's transit shape, we use the Showman et al. (2009b) model directly by deriving the wind-induced shape from contours of constant density along the planet's terminator. The resulting shape has a total radius difference of around  $\sim 700 \text{ km}$ . However, when we use our numerical lightcurve-fitting routine to estimate the detectability of this shape in a transit lightcurve, we find that it is not detectable, with lightcurve residuals of order only  $10^{-5}$  of the stellar flux.

To understand why the detectability is so low, we cal-

TABLE 1  
FOURIER COMPONENTS OF MODEL HD189733B SHAPE FROM FIGURE 4.

Fourier Component	Symmetric Amplitude	Antisymmetric Amplitude
$n = 0$	81360 km	—
$n = 1$	120.12 km	0.74 km
$n = 2$	-0.51 km	-64.78 km
$n = 3$	55.68 km	-0.31 km
$n = 4$	-0.51 km	32.45 km
$n = 5$	-4.61 km	-0.25 km
$n = 6$	-0.30 km	7.66 km

NOTE.—There is no antisymmetric component for  $n = 0$ , which corresponds to the average spherical radius. We define the  $n = 1$  shape component with  $\Psi = 0$  as “symmetric” to be consistent with the higher order components (see Figure 2, caption). What is listed as the “antisymmetric” component of  $n = 1$ , the  $\Psi = \pi/2$  component, actually produces a symmetric lightcurve as well, but is shown under that heading for consistency with the higher order shapes. See text. That all of the  $\Psi = \pi/2$  components have so little power owes to the planet’s symmetry around its own equator.

culate detectabilities for planets with regular shapes such that  $r(\theta) = R_p + A \sin(n\Theta + \Psi)$ . The  $n = 0$  term corresponds to the planet’s average radius, the  $n = 1$  term to offsets between the center of mass and center of figure, the  $n = 2$  term to planetary oblateness, and higher order terms to more complex shapes. The  $n = 1$  term is not detectable in a transit lightcurve. The projected shapes that are symmetric with respect to the planet’s orbit normal produce symmetric lightcurves; those shapes that are asymmetric produce antisymmetric lightcurves. In general shapes with lower  $n$  have higher detectabilities, and require less-fine time resolution than shapes with higher  $n$ . However the symmetric  $n = 2$  term has somewhat low detectability due to the ability of a spherical planet model to partially mimic its transit lightcurve signature.

A Fourier decomposition of the model HD189733b shape reveals why it would be so hard to detect. Most of the amplitude of the shape is in the  $n = 1$  and  $n = 2$  terms: the  $n = 1$  is undetectable, and the  $n = 2$  has relatively low detectability. The higher order terms become progressively harder to detect as  $n$  increases. Thus the smooth nature of the predicted HD189733b shape leads to its low transit detectability.

The detectability of other planets will depend on their wind velocities and zonal wind structures. However, the high insolation and low rotation rates of all hot Jupiters may drive them to behave similarly to HD189733b. Mul-

tiple counterrotating jets would avoid the low detectability of the oblateness ( $n = 2$ ) term, but higher  $n$  terms have lower detectabilities as well. Variation in the height of clouds or the absorption from haze or the atmosphere around the disk could lead to detectable shapes, but only in unusual circumstances. Hence we think that it is unlikely that the winds on transiting planets will be able to affect their lightcurves at a level that will be detectable in the near-future.

JWB and CSC were supported for this work in part by the NASA Postdoctoral Program, administered by Oak Ridge Associated Universities through a contract with NASA, at Ames Research Center and the LAPLACE Astrobiology Institute at the University of Arizona, respectively. APS was supported by a grant from the NASA Origins program. JWB acknowledges the Department of Physics at the University of Idaho for providing publication costs for this paper via startup funds.

## REFERENCES

Arnold, L. F. A. 2005, ApJ, 627, 534  
 Barnes, J. W. 2007, PASP, 119, 986  
 Barnes, J. W. & Fortney, J. J. 2003, ApJ, 588, 545  
 —. 2004, ApJ, 616, 1193

Borucki, W. J., Koch, D., Jenkins, J., Sasselov, D., Gilliland, R., Batalha, N., Latham, D. W., Caldwell, D., Basri, G., Brown, T., Christensen-Dalsgaard, J., Cochran, W. D., DeVore, E., Dunham, E., Dupree, A. K., Gautier, T., Geary, J., Gould, A., Howell, S., Kjeldsen, H., Lissauer, J., Marcy, G., Meibom, S., Morrison, D., & Tarter, J. 2009, *Science*, 325, 709

Brown, T. M., Charbonneau, D., Gilliland, R. L., Noyes, R. W., & Burrows, A. 2001, *ApJ*, 552, 699

Burrows, A., Sudarsky, D., & Hubbard, W. B. 2003, *ApJ*, 594, 545

Charbonneau, D., Allen, L. E., Megeath, S. T., Torres, G., Alonso, R., Brown, T. M., Gilliland, R. L., Latham, D. W., Mandushev, G., O'Donovan, F. T., & Sozzetti, A. 2005, *ApJ*, 626, 523

Charbonneau, D., Knutson, H. A., Barman, T., Allen, L. E., Mayor, M., Megeath, S. T., Queloz, D., & Udry, S. 2008, *ApJ*, 686, 1341

Cho, J. Y.-K., Menou, K., Hansen, B. M. S., & Seager, S. 2003, *ApJ*, 587, L117

Cooper, C. S. & Showman, A. P. 2005, *ApJ*, 629, L45

—. 2006, *ApJ*, 649, 1048

Cooper, C. S., Sudarsky, D., Milsom, J. A., Lunine, J. I., & Burrows, A. 2003, *ApJ*, 586, 1320

Deming, D., Harrington, J., Seager, S., & Richardson, L. J. 2006, *ApJ*, 644, 560

Deming, D., Seager, S., Richardson, L. J., & Harrington, J. 2005, *Nature*, 434, 740

Dobbs-Dixon, I. & Lin, D. N. C. 2008, *ApJ*, 673, 513

Fortney, J. J. 2005, *MNRAS*, 364, 649

Fortney, J. J., Cooper, C. S., Showman, A. P., Marley, M. S., & Freedman, R. S. 2006, *ApJ*, 652, 746

Fortney, J. J., Marley, M. S., Lodders, K., Saumon, D., & Freedman, R. 2005, *ApJ*, 627, L69

Grillmair, C. J., Burrows, A., Charbonneau, D., Armus, L., Stauffer, J., Meadows, V., van Cleve, J., von Braun, K., & Levine, D. 2008, *Nature*, 456, 767

Grillmair, C. J., Charbonneau, D., Burrows, A., Armus, L., Stauffer, J., Meadows, V., Van Cleve, J., & Levine, D. 2007, *ApJ*, 658, L115

Harrington, J., Hansen, B. M., Luszcz, S. H., Seager, S., Deming, D., Menou, K., Cho, J. Y.-K., & Richardson, L. J. 2006, *Science*, 314, 623

Holton, J. R. 2004, An introduction to dynamic meteorology (International geophysics series, San Diego, New York: Academic Press, —c1992, 3rd ed.)

Hubbard, W. B., Fortney, J. J., Lunine, J. I., Burrows, A., Sudarsky, D., & Pinto, P. 2001, *ApJ*, 560, 413

Hui, L. & Seager, S. 2002a, *ApJ*, 572, 540

—. 2002b, *ApJ*, 572, 540

Iro, N., Bézard, B., & Guillot, T. 2005, *A&A*, 436, 719

Knutson, H. A., Charbonneau, D., Allen, L. E., Burrows, A., & Megeath, S. T. 2008, *ApJ*, 673, 526

Knutson, H. A., Charbonneau, D., Allen, L. E., Fortney, J. J., Agol, E., Cowan, N. B., Showman, A. P., Cooper, C. S., & Megeath, S. T. 2007, *Nature*, 447, 183

Knutson, H. A., Charbonneau, D., Cowan, N. B., Agol, E., Showman, A. P., Fortney, J. J., Henry, G. W., Everett, M. E., & Allen, L. E. 2009, *ArXiv e-prints*, 802

Langton, J. & Laughlin, G. 2007, *ApJ*, 657, L113

Rauscher, E., Menou, K., Seager, S., Deming, D., Cho, J. Y.-K., & Hansen, B. M. S. 2007, *ApJ*, 664, 1199

Richardson, L. J., Deming, D., Horning, K., Seager, S., & Harrington, J. 2007, *Nature*, 445, 892

Seager, S. & Hui, L. 2002, *ApJ*, 574, 1004

Seager, S. & Sasselov, D. D. 2000, *ApJ*, 537, 916

Showman, A. P., Cooper, C. S., Fortney, J. J., & Marley, M. S. 2008, *ApJ*, 682, 559

—. 2009a, *ArXiv e-prints*, 802

Showman, A. P., Fortney, J. J., Lian, Y., Marley, M. S., Freedman, R. S., Knutson, H. A., & Charbonneau, D. 2009b, *ApJ*

Showman, A. P. & Guillot, T. 2002, *A&A*, 385, 166

Sudarsky, D., Burrows, A., & Pinto, P. 2000, *ApJ*, 538, 885

Swain, M. R., Bouwman, J., Akeson, R. L., Lawler, S., & Beichman, C. A. 2008, *ApJ*, 674, 482

Williams, P. K. G., Charbonneau, D., Cooper, C. S., Showman, A. P., & Fortney, J. J. 2006, *ApJ*, 649, 1020